Renewable Energy and Power Quality Journal
https://repqj.com/index.php/repqj/index
RE&PQJ, Vol. 23, No. 6, 2025

Probabilistic Available Transfer Capacity Calculation Using Broad Learning System and Gaussian Mixture Model-Based Clustering

Xiongguang Zhao*, Xu Ling, Jianghui Xi, Weigang Jin, Ying Wang, Peng Yuan, Xiaodong Yu

Central China Branch of State Grid Corporation of China, Wuhan, 430070, China
*Corresponding author's email: ZhaoXG_HZ@outlook.com

Abstract. This paper proposes a probabilistic available transfer capacity (ATC) calculation method by integrating a broad learning system (BLS) with Gaussian mixture model-based clustering. The key feature of this method is the development of a surrogate model for ATC calculation based on BLS. First, the deterministic ATC problem is formulated as an optimal power flow problem aimed at maximizing transmission power. Second, the joint probability distribution of uncertain renewable power generation and loads is modeled based on Copula theory, which is a powerful tool to capture their correlations. Third, an improved Gaussian mixture model-based clustering method, which combines kernel density estimation with a Gaussian component reduction strategy, is employed to generate high-quality training samples. It overcomes numerical issues encountered when using GMM to generate a sufficiently large number of training samples, which are then used to construct the BLS-based surrogate model for ATC calculation. Finally, a large number of ATC samples are efficiently generated through Monte Carlo simulation on the BLS-based surrogate model, from which the probability distribution and statistical characteristics of the ATC are derived. The proposed method is validated on the 118-bus, 300-bus, and 1354-bus systems with integrated wind and photovoltaic generation, and compared with surrogate models based on polynomial chaos expansion (PCE) and Gaussian process regression (GPR). For the 118-bus and 300-bus systems, the proposed method reduces distribution function errors to less than 50% of those from PCE and GPR methods, while maintaining high computational efficiency similar to the GPR method. For the 1354-bus system, the PCE method fails to train the model due to memory constraints, and the GPR method produces large errors. In contrast, the proposed method remains accurate and efficient, demonstrating strong scalability for large-scale probabilistic ATC problems.

Key words. probabilistic available transfer capacity, broad learning system, Gaussian mixture model, clustering, large-scale power systems.

1. Introduction

Available transfer capability (ATC) [1] is a key metric for assessing the security margin of power systems. It provides crucial information for power market participants to develop trading strategies. However, the increasing integration of renewable energy [2] and the growing electrification of energy end-use sectors [3,4] have introduced significant uncertainties to power systems, leading to variations in ATC [5,6]. In this context, probabilistic ATC (PATC) calculation [7] has emerged as a quantitative method to evaluate ATC under the influence of these uncertainties. The objective of PATC is to determine the probability distribution and statistical characteristics of ATC. However, PATC calculation remains a challenging task, particularly for large-scale power systems, due to the complex probability distributions of renewable energy generation and the strong nonlinearity of the ATC calculation model [8].

As defined in [9], ATC represents the maximum transmission power that satisfies security constraints, either between two regions or along a transmission path, minus existing transmission commitments (ETC), capacity benefit margin (CBM), and transmission reliability margin (TRM). This maximum transmission power is also referred to as the total transfer capacity (TTC). The PATC calculation to obtain the probability density function (PDF) of ATC is proposed in [2] to account for uncertainties arising from equipment unavailability. Hourly load uncertainties are considered in [3] to evaluate the PATC using statistical indices such as the expectation and percentiles. Monte Carlo simulation (MCS) is the most widely used method for PATC calculation, as presented in [2] and [3]. However, MCS requires a large number of deterministic ATC evaluations, leading to a substantial computational burden. This is because a single deterministic ATC evaluation is time-consuming, regardless of whether the repeated power flow [10], continuation power flow [11,12], or optimal power flow (OPF) [13,14] method is used.

To mitigate the computational burden of PATC, researchers have explored surrogate model-based simulation methods [15,16]. In these methods, a surrogate model of deterministic ATC calculation is established, and MCS is then performed on the surrogate model [17]. A variety of surrogate models, such as polynomial chaos expansion (PCE) [18], Gaussian process regression (GPR) [19], and low-rank approximation (LRA), are available off-the-shelf in the open-source uncertainty quantification software [20]. Ref. [15] applies PCE to calculate the PATC in power systems integrated with wind and photovoltaic power generation, where ATC is represented using a spectral expansion of orthogonal polynomials. Ref. [16] employs LRA to calculate the PATC in wind power-integrated power systems, where ATC is approximated as the sum of a limited number of rank-one tensors. Similarly, the GPR-based surrogate method can be used to calculate PATC by representing ATC as a statistical interpolation based on Gaussian processes.

While the PCE model accurately approximates ATC, the number of its coefficients increases exponentially with the input dimension. Therefore, establishing the model becomes computationally demanding when the number of uncertain variables is large. The LRA model provides a solution to overcome the curse of dimensionality, but its accuracy is lower than that of PCE when calculating PATC in a small system with low-dimensional uncertain variables. The GPR model presents a moderate computational burden for high-dimensional problems, but it also faces scalability challenges due to its lower accuracy in higher-order statistical characteristics. We observe that the expectation of ATC obtained by GPR consistently maintains high accuracy, but the errors in variance and other statistical characteristics increase significantly as the dimension of uncertain variables grows.

This paper aims to overcome the scalability limitations of existing methods by designing a broad learning system (BLS)-based surrogate model for PATC calculation. The main contributions of this paper are summarized as follows:

1) We develop a BLS-based surrogate model to calculate PATC in power systems, accounting for uncertainties in renewable energy generation and power loads. The BLS offers strong nonlinear representation capabilities and high efficiency, balancing computational burden and accuracy, even in large-scale systems.

2) We combine kernel density estimation with a density-preserving component reduction algorithm to enhance Gaussian mixture model (GMM)-based clustering. This method overcomes numerical issues that arise when applying GMM-based clustering to generate a large number of clusters for producing sufficient training samples to construct the BLS-based surrogate model.

The rest of the paper is organized as follows: Section 2 formulates the mathematical model for ATC calculation. Section 3 presents the uncertainty models of renewable energy generation and load demands in power systems, while Section 4 introduces the BLS-based PATC calculation method. Case studies are provided in Section 5, followed by conclusions in Section 6.

2. Mathematical Formulation for Available Transfer Capacity

The deterministic ATC evaluation serves as the foundation for PATC calculation. In this study, the OPF-based method is employed to evaluate ATC, where the problem is formulated as follows:

$$\mathrm{ATC} = \max_{\{\lambda,\Delta P_{G,f},\Delta Q_{G,f}\}} \lambda \sum\nolimits_{t\in\mathbb{T}} P_{L,t}^{\mathrm{init}} \quad (1)$$

$$\text{s.t. } P_i = \sum_{j\in\mathbb{I}} V_i V_j \left[G_{ij}\cos\left(\theta_i-\theta_j\right) + B_{ij}\sin\left(\theta_i-\theta_j\right)\right], \forall i \in \mathbb{I} \quad (2)$$

$$Q_i = \sum_{j\in\mathbb{I}} V_i V_j \left[G_{ij}\sin\left(\theta_i-\theta_j\right) - B_{ij}\cos\left(\theta_i-\theta_j\right)\right], \forall i \in \mathbb{I} \quad (3)$$

$$P_i = P_{\mathrm{G},i} + P_{\mathrm{WT},i} + P_{\mathrm{PV},i} - P_{\mathrm{L},i}, \forall i \in \mathbb{I} \quad (4)$$

$$Q_i = Q_{\mathrm{G},i} + Q_{\mathrm{WT},i} + Q_{\mathrm{PV},i} - Q_{\mathrm{L},i}, \forall i \in \mathbb{I} \quad (5)$$

$$P_{\mathrm{G},f} = P_{\mathrm{G},f}^{\mathrm{init}} + \Delta P_{\mathrm{G},f}, \forall f \in \mathbb{F} \quad (6)$$

$$Q_{\mathrm{G},f} = Q_{\mathrm{G},f}^{\mathrm{init}} + \Delta Q_{\mathrm{G},f}, \forall f \in \mathbb{F} \quad (7)$$

$$P_{\mathrm{L},t} = \left(1+\lambda\right) P_{\mathrm{L},t}^{\mathrm{init}}, \forall t \in \mathbb{T} \quad (8)$$

$$Q_{\mathrm{L},t} = \left(1+\lambda\right) Q_{\mathrm{L},t}^{\mathrm{init}}, \forall t \in \mathbb{T} \quad (9)$$

$$P_{\mathrm{G},f}^{\mathrm{L}} \le P_{\mathrm{G},f} \le P_{\mathrm{G},f}^{\mathrm{U}}, \forall f \in \mathbb{F} \quad (10)$$

$$Q_{\mathrm{G},f}^{\mathrm{L}} \le Q_{\mathrm{G},f} \le Q_{\mathrm{G},f}^{\mathrm{U}}, \forall f \in \mathbb{F} \quad (11)$$

$$V_i^{\mathrm{L}} \le V_i \le V_i^{\mathrm{U}}, \forall i \in \mathbb{I} \quad (12)$$

$$\theta_i^{\mathrm{L}} \le \theta_i \le \theta_i^{\mathrm{U}}, \forall i \in \mathbb{I} \quad (13)$$

$$I_{ij}^{\mathrm{L}} \le h_{ij}\left(V_i,\theta_i,V_j,\theta_j,G_{ij},B_{ij},b_{ij}\right) \le I_{ij}^{\mathrm{U}}, \forall ij \in \mathbb{L} \quad (14)$$

where V_i and θ_i, and V_j and θ_j are the magnitudes and angles of nodal voltages at bus i and j, respectively; G_{ij} and B_{ij} are the real and imaginary parts of the element in the i_{th} row and j_{th} column of the nodal admittance matrix, respectively; P_i and Q_i are the active and reactive nodal power injections at bus i, respectively; $P_{\mathrm{G},i}$, $P_{\mathrm{WT},i}$, and $P_{\mathrm{PV},i}$ are the active power outputs of conventional, wind turbine (WT), and photovoltaic (PV) power generation at bus i,

respectively, while $Q_{\mathrm{G},i}$, $Q_{\mathrm{WT},i}$, and $Q_{\mathrm{PV},i}$ are the corresponding reactive power outputs, $P_{\mathrm{L},i}$ and $Q_{\mathrm{L},i}$ are the active and reactive power loads at bus i , respectively; $P_{\mathrm{G},f}^{\mathrm{init}}$ and $Q_{\mathrm{G},f}^{\mathrm{init}}$ are the active and reactive power outputs of conventional power generation at bus f in the base state, while $\Delta P_{\mathrm{G},f}$ and $\Delta Q_{\mathrm{G},f}$ are the adjustments in the active and reactive power of conventional power generation at bus f to balance the increased power load in the receiving region; $P_{\mathrm{L},t}^{\mathrm{init}}$ and $Q_{\mathrm{L},t}^{\mathrm{init}}$ are the active and reactive power loads at bus t in the base state; $\mathbb{I}$ is the set of all buses in the power system, and $\mathbb{F}$ and $\mathbb{T}$ are the sets of buses in the sending and receiving regions, respectively, $\mathbb{L}$ is the set of all branches in the power system; λ is the load increase factor in the receiving regions, when $\lambda = 0$ corresponds to the base state; $P_{\mathrm{G},f}^{\mathrm{U}}$, $P_{\mathrm{G},f}^{\mathrm{L}}$ and $Q_{\mathrm{G},f}^{\mathrm{U}}$, $Q_{\mathrm{G},f}^{\mathrm{L}}$ are the upper and lower limits of $P_{\mathrm{G},f}$ and $Q_{\mathrm{G},f}$, respectively; V_i^{U} , V_i^{L} and θ_i^{U} , θ_i^{L} are the upper and lower limits of V_i and θ_i , respectively, where $\theta_i^{\mathrm{U}} = \theta_i^{\mathrm{L}} = \theta_{\mathrm{ref}}$ when i is the reference bus; $h_{ij}(\cdot)$ is the function to calculate branch current magnitude at branch ij , I_{ij}^{U} and I_{ij}^{L} are the upper and lower limits of the current magnitudes at branch ij .

The objective function is to maximize the incremental transmission power from the sending region to the receiving region, based on the ETC (i.e., the base state), where the decision variables are λ , $\Delta P_{\mathrm{G},f}$ and $\Delta Q_{\mathrm{G},f}$. Constraints (2)-(5) represent the nonlinear power flow equations based on polar coordinates. Constraints (6)-(9) describe the increased power load in the receiving region and the corresponding power generation adjustments in the sending region. Constraints (10)-(14) are the security constraints of the power system. The optimal value of the objective function represents the ATC without consideration of CBM and TRM. In this study, the IPOPT [21], an open-source primal-dual interior-point method solver, is used to solve the nonlinear optimization problem.

3. Probability Models of Renewable Power Generation and Load Demand

In this study, we aim to a probabilistic assessment of ATC under the influence of uncertainties in renewable power generation and load demand. Accurate probabilistic modeling of these uncertainties is a prerequisite for PATC calculation. Notably, the correlation among these uncertain variables cannot be overlooked, because it has a significant impact on system states. Therefore, in this section, we first model the marginal distributions of individual uncertain variables and then construct their joint probability distribution using Copula theory.

A. Marginal Probability Distribution

Wind speed is the primary source of uncertainty in WT power generation. Let v_i denote the wind speed of the WT power generation at bus i , and let v denote the vector comprising all v_i . The uncertainty of v_i is commonly described by a Weibull distribution, whose PDF is given by:

$$f_{v_i}(v_i) = \begin{cases} \dfrac{\beta_i}{\alpha_i}\left(\dfrac{v_i}{\alpha_i}\right)^{\beta_i - 1} \mathrm{e}^{-(v_i/\alpha_i)^{\beta_i}}, & v_i \geq 0 \\ 0, & v_i < 0 \end{cases} \quad (15)$$

where α_i and β_i are the scale and shape parameters, respectively.

Solar irradiation is the primary source of uncertainty in PV power generation. Let γ_i denote the solar irradiation of the PV power generation at bus i , and let γ denote the vector comprising all γ_i . The uncertainty of γ_i is commonly described by a Beta distribution, whose PDF is given by:

$$f_{\gamma_i}(\gamma_i) = \begin{cases} \dfrac{(\gamma_i - a_i)^{\gamma_i - 1}(b_i - \gamma_i)^{s_i - 1}}{(b_i - a_i)^{\gamma_i + s_i - 1}\mathrm{B}(r_i, s_i)}, & \gamma_i \in [a_i, b_i] \\ 0, & \gamma_i \notin [a_i, b_i] \end{cases} \quad (16)$$

where a_i and b_i are the parameters representing the minimum and maximum values of γ_i , r_i and s_i are the shape parameters, and $\mathrm{B}(\cdot)$ is the Beta function.

Let $P_{\mathrm{L},i}$ denote the active power of load demand at bus i , and let $\boldsymbol{P}_{\mathrm{L}}$ denote the vector comprising all $P_{\mathrm{L},i}$. The uncertainty of $P_{\mathrm{L},i}$ is commonly described by a Gaussian distribution, whose PDF is given by:

$$f_{P_{\mathrm{L}}}(P_{\mathrm{L},i}) = \frac{1}{\sigma_i\sqrt{2\pi}} \mathrm{e}^{-(P_{\mathrm{L},i} - \mu_i)^2 / (2\sigma_i^2)} \quad (17)$$

where μ_i and σ_i are the mean and standard deviation, respectively.

B. Copula-Based Joint Probability Distribution

The uncertain variable vector is denoted as $\boldsymbol{u}$, which is formed by the wind speed vector $\boldsymbol{v}$, solar irradiation vector γ , and the load vector $\boldsymbol{P}_{\mathrm{L}}$. The marginal probability distributions of the uncertain variable vector $\boldsymbol{x}$ are established in (15)-(17). To further describe their correlation, the joint cumulant distribution function (CDF) is established based on Copula theory, as given below:

$$F(u_1,\cdots,u_n)=C\left(F_1(u_1),\cdots,F_n(u_n)\right) \quad (18)$$

where $u_1,u_2,\cdots,u_n$ represent the elements of $\boldsymbol{u}$, i.e., $\boldsymbol{u}=[u_1,u_2,\cdots,u_n]=\left[\boldsymbol{v}^{\mathrm{T}},\gamma^{\mathrm{T}}\boldsymbol{P}_{\mathrm{L}}^{\mathrm{T}}\right]$, $F(\cdot)$ represents CDF, and $C(\cdot)$ is the Copula function. Thus, the joint PDF of $\boldsymbol{u}$ is derived as:

$$f(u_1,\cdots,u_n)=c\left(F_1(u_1),\cdots,F_n(u_n)\right)\cdot f_1(u_1)\cdot\cdots f_n(u_n) \quad (19)$$

where $c(\cdot)$ is the Copula density function. In this study, the Gaussian Copula function is used.

The parameters of the Copula function and the marginal distribution functions are determined using the maximum likelihood estimation method with historical data, the detailed steps can be found in [20].

4. Probabilistic ATC Calculation

In this section, the definition of PATC and its simulation-based calculation method are reviewed. Then, a broad learning system-based surrogate model for ATC calculation is developed. Next, an improved GMM-based clustering method is designed to generate high-quality training samples for constructing the ATC surrogate model. Finally, the complete PATC calculation process is presented.

A. Definition and Simulation-Based Calculation Method for PATC

The transformations from wind speed v_i to $P_{\mathrm{WT},i}$ and from solar irradiation γ_i to $P_{\mathrm{PV},i}$ can be obtained based on WT and PV power models [22], respectively. Due to the uncertainties in wind speed and solar irradiation, the variables $P_{\mathrm{WT},i}$ and $P_{\mathrm{PV},i}$ are uncertain. Recalling problem (1)-(14), changes in $P_{\mathrm{WT},i}$, $P_{\mathrm{PV},i}$, and $P_{\mathrm{L},I}$ lead to variation in the optimal objective function value, ATC. Therefore, ATC becomes an uncertain variable influenced by these input uncertainties. The goal of PATC calculation is to determine the probability distribution and statistical characteristics of ATC.

Let Y and $\hat{Y}$ denote the ATC without and with consideration of CBM and TRM, respectively. Figure 1(a) and Figure 1(b) illustrate the PDFs of Y and $\hat{Y}$, respectively. Since CBM and TRM are fixed margins determined by system operators, and their determination methods are not standardized, this study focuses on accurately obtaining the probability distribution and statistical indices of ATC without incorporating CBM and TRM. Once CBM and TRM are specified, further PATC-related calculations, whether for the PDF or statistical indices, can be carried out by simply subtracting CBM and TRM. The relationships between the PDF and statistical characteristics of Y and those of $\hat{Y}$ are provided in (20)-(23).

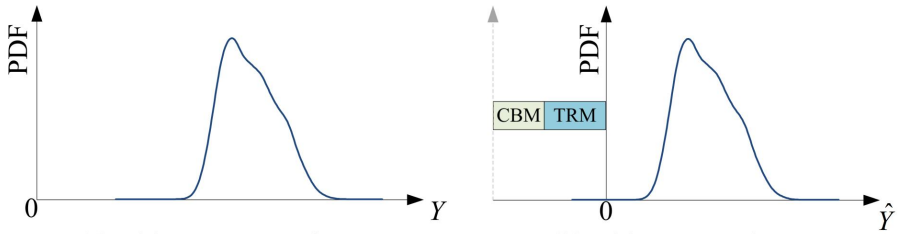

(a) without CBM and TRM (b) with CBM and TRM

Figure 1. PDFs of ATC without and with CBM and TRM.

$$f_{\widehat{\mathrm{ATC}}}\left(\hat{Y}\right)=f_{\mathrm{ATC}}\left(\hat{Y}+\mathrm{TRM}+\mathrm{CBM}\right) \quad (20)$$

$$E\left(\hat{Y}\right)=E(Y)-\mathrm{TRM}-\mathrm{CBM} \quad (21)$$

$$\mathrm{Std}\left(\hat{Y}\right)=\mathrm{Std}(Y) \quad (22)$$

$$q_\tau\left(\hat{Y}\right)=q_\tau(Y)-\mathrm{TRM}-\mathrm{CBM} \quad (23)$$

where $f(\cdot)$, $E(\cdot)$, $\mathrm{Std}(\cdot)$, and $q_\tau(\cdot)$ are probability density, expectation, standard deviation, and τ-percentile functions, respectively.

Let $\boldsymbol{P}_{\mathrm{WT}}$, $\boldsymbol{P}_{\mathrm{PV}}$, and $\boldsymbol{P}_{\mathrm{L}}$ denote the vector comprising all $P_{\mathrm{WT},i}$, $P_{\mathrm{PV},i}$, and $P_{\mathrm{L},i}$, respectively. The corresponding reactive powers are assumed to be controlled by constant power factors. The ATC is expressed as the optimal value function $Y=\Gamma\left(\boldsymbol{P}_{\mathrm{WT}},\boldsymbol{P}_{\mathrm{PV}},\boldsymbol{P}_{\mathrm{L}}\right)$, where $\Gamma(\cdot)$ represents the solution to the optimization problem (1)-(14). Since the function $\Gamma(\cdot)$ is nonlinear and lacks a closed-form expression, deriving the PDF of ATC directly from the given joint PDF of the uncertain variable vector $\boldsymbol{u}$ is challenging. Therefore, the MCS method is employed to estimate the PATC. For each realization of the uncertain variables, solving the OPF problem (1)-(14) yields a corresponding realization of the uncertain ATC. Based on these ATC samples, the PDF and statistical characteristics of ATC are estimated. However, the computational burden of performing a large number of MCS on the OPF-based ATC calculation model is significantly heavy.

B. BLS-Based Surrogate Model for ATC Calculation

The broad learning system [23,24] is a novel neural network that focuses on increasing the breadth rather than the depth. The BLS exhibits remarkable computational efficiency and generalization ability in high-dimensional nonlinear representations. The effectiveness of BLS in regression tasks has been demonstrated in existing literature [25-28]. Therefore, we introduce it to establish the surrogate model of ATC for PATC calculation. Figure 2 illustrates the neural network structure of the BLS-based surrogate model of ATC. The input $\boldsymbol{X}$ is the nodal active power injection vector associated with the uncertain powers from WT power generation, PV power generation, and load demands, while the output Y is the ATC. The hidden layer consists of two parts: 1) a feature mapping layer, and 2) an enhancement layer.

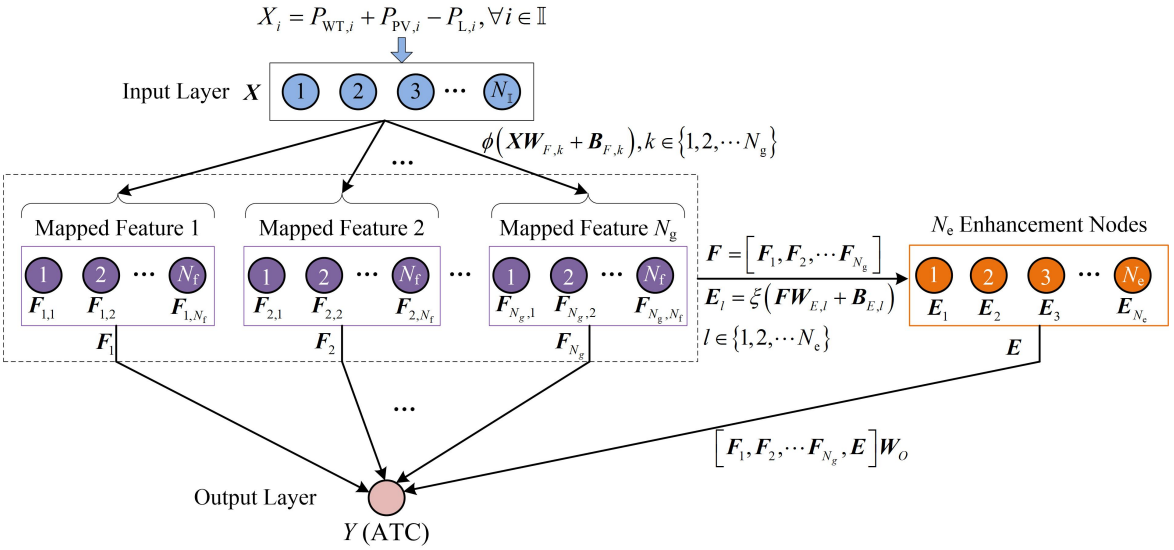

Figure 2. Neural network structure of the BLS-based surrogate model of ATC.

The feature mapping layer consists of N_{g} groups of feature mapping units. For the k_{th} mapping unit, an N_{f}-dimensional feature is mapped from input $\boldsymbol{X}$ by:

$$\boldsymbol{F}_k = \phi\left(\boldsymbol{X}\boldsymbol{W}_{F,k} + \boldsymbol{B}_{F,k}\right) \quad (24)$$

where $\boldsymbol{W}_{F,k}$ and $\boldsymbol{B}_{F,k}$ are the linear mapping coefficient vectors, randomly generated between -1 and 1, and $\phi(\cdot)$ is a nonlinear mapping operator, which is an implicit function based on a sparse autoencoder [29]. Specifically, the sparse autoencoder is implemented by solving the following problem:

$$\arg\min_{\hat{\boldsymbol{W}}_{F,K}} \left\| \left[\boldsymbol{X}, \boldsymbol{B}_{F,k}\right]\hat{\boldsymbol{W}}_{F,k} - \left(\boldsymbol{X}\boldsymbol{W}_{F,k} + \boldsymbol{B}_{F,k}\right) \right\|_2^2 + \lambda \left\| \hat{\boldsymbol{W}}_{F,k} \right\|_1 \quad (25)$$

where $\hat{\boldsymbol{W}}_{F,k}$ is the decision variable, and λ is the regularization term coefficient. This problem represents the least squares solution $\hat{\boldsymbol{W}}_{F,k}$ of the equation $\left[\boldsymbol{X}, \boldsymbol{B}_{F,k}\right]\hat{\boldsymbol{W}}_{F,k} = \left(\boldsymbol{X}\boldsymbol{W}_{F,k} + \boldsymbol{B}_{F,k}\right)$ with an L1 regularization term. The alternating direction method of multipliers algorithm is used to solve this problem, and the detailed iteration steps can be found in [29]. Therefore, $\boldsymbol{F}_k = \phi\left(\boldsymbol{X}\boldsymbol{W}_{F,k} + \boldsymbol{B}_{F,k}\right) = \left[\boldsymbol{X}, \boldsymbol{B}_{F,k}\right]\hat{\boldsymbol{W}}_{F,k}$. This represents the sparse and compact features obtained by applying the implicit function $\phi(\cdot)$, which is realized by solving the problem (25) to fine-tune the features obtained from the randomly linear mapping $\boldsymbol{X}\boldsymbol{W}_{F,k} + \boldsymbol{B}_{F,k}$.

The enhancement layer contains N_e enhancement nodes, and their input is the concatenation of the mapped features $\left[\boldsymbol{F}_1, \boldsymbol{F}_2, \cdots, \boldsymbol{F}_{N_{\mathrm{g}}}\right]$, denoted as $\boldsymbol{F}$. For the l_{th} enhancement node, its output $\boldsymbol{E}_l$ is mapped from $\boldsymbol{F}$ as:

$$\boldsymbol{E}_l = \xi\left(\boldsymbol{F}\boldsymbol{W}_{E,l} + \boldsymbol{B}_{E,l}\right) \quad (26)$$

where $\boldsymbol{W}_{E,l}$ and $\boldsymbol{B}_{E,l}$ are linear mapping coefficient vectors randomly generated in the same way as $\boldsymbol{W}_{F,k}$ and $\boldsymbol{B}_{F,k}$, and $\xi(\cdot)$ is a nonlinear mapping function designed as:

$$\xi(x) = \frac{2}{1 + \mathrm{e}^{-2x}} - 1 \quad (27)$$

Based on the outputs of the feature mapping layer and the enhancement layer, the final output Y (i.e. ATC) of the BLS is calculated as:

$$Y = \left[\boldsymbol{F}, \boldsymbol{E}\right]\boldsymbol{W}_O \quad (28)$$

where $\boldsymbol{E} = \left[\boldsymbol{E}_1, \boldsymbol{E}_2, \cdots, \boldsymbol{E}_{\mathrm{Ne}}\right]$, and $\boldsymbol{W}_O$ is the weight coefficient vector that maps $\boldsymbol{F}$ and $\boldsymbol{E}$ to the output Y.

Training the BLS-based ATC surrogate model only requires determining the coefficient vector $\boldsymbol{W}_O$, since $\boldsymbol{W}_{F,k}$, $\boldsymbol{W}_{F,k}$, $\boldsymbol{W}_{E,l}$, and $\boldsymbol{B}_{E,l}$ are generated randomly and remain fixed. The training of $\boldsymbol{W}_O$ is formulated as the following optimization problem:

$$\arg\min_{\boldsymbol{W}_O} \left\| \tilde{\boldsymbol{H}} W_O - \tilde{Y} \right\|_2^2 \quad (29)$$

where $\tilde{\boldsymbol{H}}$ represents the sample matrix of the hidden layer output $[\boldsymbol{F}, \boldsymbol{E}]$ when the training samples $\tilde{\boldsymbol{X}}$ are used as input, and $\tilde{\boldsymbol{Y}}$ is the corresponding target output samples of the ATC model used for training. This problem can be efficiently solved using the pseudo-inverse operation:

$$\boldsymbol{W}_O = \tilde{\boldsymbol{H}}^{\dagger} \tilde{\boldsymbol{Y}} \quad (30)$$

where $\tilde{\boldsymbol{H}}^{\dagger}$ is the pseudo-inverse operation of $\tilde{\boldsymbol{H}}$.

C. GMM-Based Clustering for Generating Training Samples

The selection of training samples is crucial for constructing an accurate surrogate model. The GMM-based clustering is a powerful method that identifies clusters based on the probabilistic distribution of the data. Therefore, we adopt GMM-based clustering to generate high-quality training samples. However, in this context, the number of required training samples is typically on the order of 100-1000, which is significantly larger than the number of clusters in conventional clustering tasks. When attempting to estimate the parameters of a GMM with such a large number of components using the classical expectation-maximization (EM) algorithm, numerical ill-conditioning issues often arise. To address this challenge, we propose an improved GMM-based clustering approach that incorporates kernel density estimation (KDE) and a component reduction strategy.

First, N_t samples of input $\boldsymbol{X}$ are generated based on (19) and the power generation models of WT and PV, where N_t is a large number. These samples are denoted as $\{\boldsymbol{X}_1, \cdots, \boldsymbol{X}_k, \cdots, \boldsymbol{X}_{N_t}\}$, which will be used to perform MCS on the BLS-based surrogate model to generate N_{t} ATC simulation samples.

Second, based on the input samples $\{\boldsymbol{X}_1, \cdots, \boldsymbol{X}_k, \cdots, \boldsymbol{X}_{N_t}\}$, the joint PDF of $\boldsymbol{X}$ is estimated using KDE with a Gaussian kernel function, which is expressed as:

$$f_{\mathrm{KDE}}(\boldsymbol{X}) = \frac{1}{N} \sum_{k=1}^{N_t} K_{\boldsymbol{H}}(\boldsymbol{X} - \boldsymbol{X}_k) \quad (31)$$

where $K_{\boldsymbol{H}}(\cdot)$ is the Gaussian kernel function, and $\boldsymbol{H}$ is the bandwidth matrix, which is determined by Silverman's rule of thumb, as stated below:

$$\begin{cases} \boldsymbol{H} = \mathrm{diag}\left(\left[h_1^2, \cdots, h_d^2, \cdots, h_D^2 \right]^{\mathrm{T}} \right) \\ h_d = 0.9 \min\left(\sigma_d, \dfrac{IQR_d}{1.34} \right) N_t^{-0.2}, \forall d \in \{1, \cdots, D\} \end{cases} \quad (32)$$

where $\mathrm{diag}(\cdot)$ is the operator that transforms a vector into a diagonal matrix, D is the dimension of input $\boldsymbol{X}$, and σ_d and IQR_d are the standard deviation and interquartile range of the samples of input $\boldsymbol{X}$ in the d_{th} dimension, respectively.

The joint PDF obtained by KDE is treated as the base GMM, which is given by:

$$f^{(b)}(\boldsymbol{X}) = \sum_{k=1}^{K_b} \omega_k^{(b)} \mathrm{N}\left(\boldsymbol{X} \middle| \boldsymbol{\mu}_k^{(b)}, \Sigma_k^{(b)} \right) \quad (33)$$

where K_{b} is the number of Gaussian components, $\omega_k^{(\mathrm{b})}$, $\boldsymbol{\mu}_k^{(\mathrm{b})}$, and $\Sigma_k^{(b)}$ are the weight coefficient, mean vector, and covariance matrix of the k_{th} component, respectively, $\mathrm{N}(\cdot)$ is the joint PDF of the Gaussian distribution, and the symbol b indicates that the parameters belong to the base GMM. According to the parameters in (31), the parameters in (33) are obtained as follows: $K_{\mathrm{b}} = N_t$, $\omega_k^{(\mathrm{b})} = 1/N_t$, $\boldsymbol{\mu}_k^{(\mathrm{b})} = \boldsymbol{X}_k$, and $\Sigma_k^{(b)} = \boldsymbol{H}$.

Next, a density-preserving component reduction algorithm is developed to obtain a simplified GMM with $K_r \left(K_r < K_b = N_t \right)$ Gaussian components. The simplified GMM is denoted as:

$$f^{(r)}(\boldsymbol{X}) = \sum_{\ell=1}^{K_r} \omega_\ell^{(r)} \mathrm{N}\left(\boldsymbol{X} \middle| \boldsymbol{\mu}_\ell^{(r)}, \Sigma_\ell^{(r)} \right) \quad (34)$$

where K_{r} is the number of reduced Gaussian components, $\omega_\ell^{(\mathrm{r})}$, $\boldsymbol{\mu}_\ell^{(\mathrm{r})}$, and $\Sigma_\ell^{(r)}$ are the weight coefficient, mean vector, and covariance matrix of the ℓ_{th} component, respectively. The density-preserving component reduction problem for obtaining (34) is formulated as:

$$\max_{\left(\omega_\ell^{(r)}, \boldsymbol{\mu}_\ell^{(r)}, \Sigma_\ell^{(r)}\right)} \left\{ \mathrm{E}_{\chi \sim f^{(b)}(\boldsymbol{X})} \left[\ln f^{(r)}(\chi) \right] \right\} \quad (35)$$

where $\boldsymbol{\chi}$ represents the virtual samples following the probability distribution in (33). The decision variables are the parameters $\omega_\ell^{(\mathrm{r})}$, $\boldsymbol{\mu}_\ell^{(\mathrm{r})}$, and $\Sigma_\ell^{(r)}$ of (34), and the objective function is to maximize the log-likelihood of $\boldsymbol{\chi}$ under the simplified GMM. This problem is solved using the variational approximation method. The detailed derivation can be found in [30], and the iterative calculation also involves E-step and M-step. To avoid numeric overflow due to the large number K_b, an improved E-step [31] is adopted. The calculation

expressions for the E-step and M-step are presented as follows:

E-step:

$$\Re_{k,\ell}=1/2\begin{Bmatrix}\left(\boldsymbol{\mu}_k^{(b)}-\boldsymbol{\mu}_\ell^{(r)}\right)^{\mathrm{T}}\left(\sum_\ell^{(r)}\right)^{-1}\left(\mu_k^{(b)}-\mu_\ell^{(r)}\right)\\+\mathrm{tr}\left[\left(\sum_\ell^{(r)}\right)^{-1}\sum_k^{(b)}\right]+\ln\left|\sum_\ell^{(r)}\right|\end{Bmatrix} \quad (36)$$

$$l_{k,\min}=\arg\min_l\left(\Re_{k,l}\right),\ l=1,2,\cdots,K_{\mathrm{r}} \quad (37)$$

$$z_{k\ell}=\frac{\omega_\ell^{(\mathrm{r})}\exp\left[m\left(\Re_{k,l_{k,\min}}\right)\Re_{k,\ell}\right]}{\sum_{l=1}^{K_{\mathrm{r}}}\omega_l^{(\mathrm{r})}\exp\left[m\left(\Re_{k,l_{k,\min}}\right)\Re_{i,l}\right]} \quad (38)$$

M-step:

$$\omega_\ell^{(\mathrm{r})}=\sum_{k=1}^{K_b}z_{k\ell}\omega_k^{(\mathrm{b})} \quad (39)$$

$$\boldsymbol{\mu}_\ell^{(\mathrm{r})}=1/\omega_\ell^{(\mathrm{r})}\sum_{k=1}^{K_b}z_{k\ell}\omega_k^{(\mathrm{b})}\boldsymbol{\mu}_k^{(\mathrm{b})} \quad (40)$$

$$\sum_\ell^{(r)}=\frac{1}{\omega_\ell^{(\mathrm{r})}}\sum_{k=1}^{K_b}z_{k\ell}\omega_k^{(\mathrm{b})}\left[\sum_k^{(b)}+\left(\boldsymbol{\mu}_k^{(\mathrm{b})}-\boldsymbol{\mu}_\ell^{(\mathrm{r})}\right)\left(\boldsymbol{\mu}_k^{(\mathrm{b})}-\boldsymbol{\mu}_\ell^{(\mathrm{r})}\right)^{\mathrm{T}}\right] \quad (41)$$

where $z_{k\ell}$ ($k\in\{1,...,K_{\mathrm{b}}\},\ell\in\{1,...,K_{\mathrm{r}}\}$) is the variational parameter, $\mathrm{tr}(\cdot)$ is the trace operator for a matrix, and m is the number of virtual samples χ , which is typically set to 10 K_b , as in [30] and [31].

Finally, all the density centers of each component of $f^{(\mathrm{r})}(\boldsymbol{X})$ are collected as the training samples for the input $\boldsymbol{X}$, i.e., $\tilde{\boldsymbol{X}}=[\boldsymbol{\mu}_1^{(\mathrm{r})},...,\boldsymbol{\mu}_\ell^{(\mathrm{r})},...,\boldsymbol{\mu}_{K_{\mathrm{r}}}^{(\mathrm{r})}]$. For each training sample in $\tilde{\boldsymbol{X}}$, the corresponding ATC is obtained by solving the OPF-based ATC model (1)-(14), i.e., $\tilde{\boldsymbol{Y}}=[\tilde{Y}_1,...,\tilde{Y}_\ell,...,\tilde{Y}_{K_{\mathrm{r}}}]$.

D. Solution Procedure

Step 1: Establish the joint PDF of the uncertain variable vector $\boldsymbol{u}$ in the power system, according to the method presented in Section 3.

Step 2: Generate N_t samples of the uncertain variables based on their joint PDF using a low-discrepancy sequence. Transform these into power vector samples $\{\boldsymbol{P}_{\mathrm{WT},1},\cdots,\boldsymbol{P}_{\mathrm{WT},k},\cdots,\boldsymbol{P}_{\mathrm{WT},N_t}\}$, $\{\boldsymbol{P}_{PV,1},\cdots,\boldsymbol{P}_{PV,k},\cdots,\boldsymbol{P}_{PV,N_t}\}$, and $\{\boldsymbol{P}_{L,1},\ldots,\boldsymbol{P}_{L,k},\ldots,\boldsymbol{P}_{L,N_t}\}$ based on the WT and PV power models [22].

Step 3: Convert the power vector samples into input samples $\{\boldsymbol{X}_1,\cdots,\boldsymbol{X}_k,\cdots,\boldsymbol{X}_{N_t}\}$ for the BLS-based ATC surrogate model. Specifically, for the k_{th} input samples: $\boldsymbol{X}_k=\boldsymbol{P}_{WT,k}+\boldsymbol{P}_{PV,k}-\boldsymbol{P}_{L,k}$.

Step 4: Generate K_{r} training samples of input $\boldsymbol{X}$ and corresponding output Y for training the BLS-based ATC surrogate model, using the improved GMM-based clustering method proposed in Section 4.C. The obtained training samples are $\tilde{\boldsymbol{X}}=[\boldsymbol{\mu}_1^{(\mathrm{r})},...,\boldsymbol{\mu}_\ell^{(\mathrm{r})},...,\boldsymbol{\mu}_{K_{\mathrm{r}}}^{(\mathrm{r})}]$ and $\tilde{\boldsymbol{Y}}=[\tilde{Y}_1,...,\tilde{Y}_\ell,...,\tilde{Y}_{K_{\mathrm{r}}}]$, corresponding to the input and output, respectively.

Step 5: Establish the BLS-based ATC surrogate model using the training samples $\tilde{\boldsymbol{X}}=[\boldsymbol{\mu}_1^{(\mathrm{r})},...,\boldsymbol{\mu}_\ell^{(\mathrm{r})},...,\boldsymbol{\mu}_{K_{\mathrm{r}}}^{(\mathrm{r})}]$ and $\tilde{\boldsymbol{Y}}=[\tilde{Y}_1,...,\tilde{Y}_\ell,...,\tilde{Y}_{K_{\mathrm{r}}}]$, following the method proposed in Section 5.B.

Step 6: Generate ATC simulation results $\{Y_1,\cdots,Y_k,\cdots,Y_{N_t}\}$ by performing MCS on the BLS-based ATC surrogate model using the input samples $\{\boldsymbol{X}_1,\cdots,\boldsymbol{X}_k,\cdots,\boldsymbol{X}_{N_t}\}$.

Step 7: Estimate the PDF of ATC using the simulation samples $\{Y_1,\cdots,Y_k,\cdots,Y_{N_t}\}$ and KDE. Calculate statistical indices such as the expectation, standard deviation, and percentiles.

5. Case Studies

The 118-bus, 300-bus, and 1354-bus power systems [32], integrated with WT and PV power units, are used to evaluate the performance of the proposed method. Six, twelve, and sixty-five WT power units are connected to the 118-bus, 300-bus, and 1354-bus systems, respectively, with installed capacities of 200 MW, 40 MW, and 200 MW per unit. Similarly, six, twelve, and sixty-five PV units are integrated into the corresponding systems, with installed capacities of 100 MW, 20 MW, and 60 MW per unit.

The uncertainties of WT and PV power units, as well as all loads, are taken into account. The results obtained by the MCS using the original OPF-based ATC calculation model and a low-discrepancy sequence are used as benchmarks, whose number of simulation samples is 10000. The performances of the PCE-based and GPR-based surrogate models are compared against that of the proposed BLS-based surrogate model. The PCE and GPR methods are implemented using the UQLab toolbox [20]. For BLS-based, PCE-based, and GPR-based surrogate model method, the number of training and simulation samples is set to 1000 and 10000, respectively.

The proposed method is developed in MATLAB 2020a, and all simulations are carried out on a desktop computer equipped with an Intel i5-8400 2.8 GHz CPU and 32 GB of RAM.

A. Comparison of Probability Distribution Function Accuracy

Figures 3-5 show the PDFs and CDFs of ATC in the 118-bus, 300-bus, and 1354-bus systems obtained by different methods, respectively. The results obtained by the BLS method closely match those obtained by the MCS method and outperform those from the PCE and GPR methods. The dimensions of the uncertain variables in the 118-bus, 300-bus, and 1354-bus systems are 111, 224, and 803, respectively. It is observed that the GPR-based ATC surrogate model tends to output the mean value as the dimensionality of the problem increases. In particular, the PDF of ATC in the 1354-bus system contains an impulse at the mean, indicating that the GPR model loses its ability to represent distributional features. As a result, the accuracy of the PDF and CDF generated by the GPR method decreases significantly with increasing system scale. In contrast, the PDF and CDF accuracy of the PCE method does not deteriorate as noticeably when the system scale increases, as can be observed by comparing the results for the 300-bus and 118-bus systems. However, an out-of-memory error occurs during the training of the PCE model in the 1354-bus system. Therefore, Figure 5 does not include the PDF and CDF of ATC obtained using the PCE method.

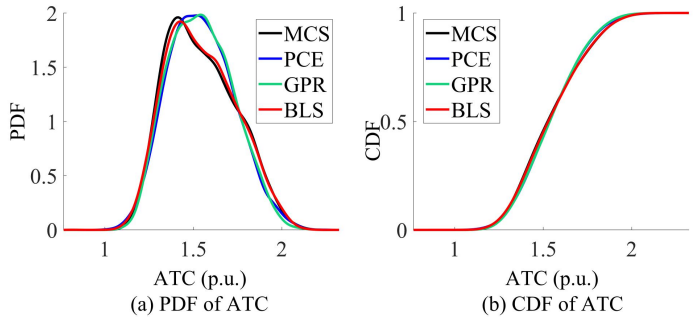

Figure 3. PDFs and CDFs of ATC in 118-bus system obtained by different methods.

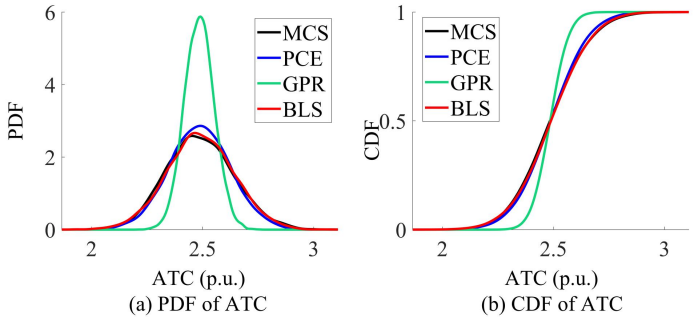

Figure 4. PDFs and CDFs of ATC in 300-bus system obtained by different methods.

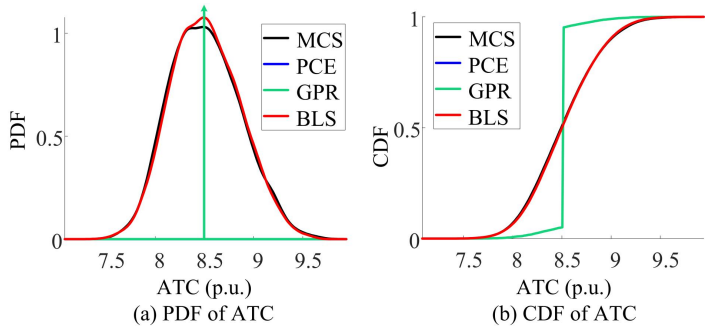

Figure 5. PDFs and CDFs of ATC in 1354-bus system obtained by different methods.

Table 1-Table3 show the PDF and CDF errors of ATC obtained by different methods, with error indices including root mean square error (RMSE), mean absolute error (MAE), and weighted absolute percentage error (WAPE). These errors are statistically evaluated based on 200 uniformly sampled points within the domain of their definition. In all three systems, the PDF and CDF errors of the proposed BLS method are less than 50% of those of the PCE and GPR methods. It is worth noting that, since the PDF calculated by the GPR method is an impulse function, its PDF error is not measured in the 1354-bus system. Meanwhile, the construction of the PCE model fails in the 1354-bus system, making it unable to complete the PATC calculation. In contrast, the proposed BLS method is capable of accurately obtaining the PDF and CDF even in large-scale systems, thereby overcoming the scalability limitations encountered by the PCE and GPR methods in PATC calculations.

Table 1. Errors of probability distribution functions of atc in the 118-bus system obtained by different methods.

Method	PDF Error			CDF Error		
	RMSE	MAE	WAPE	RMSE	MAE	WAPE
PCE	1.38E-1	9.15E-2	14.31%	1.50E-2	9.19E-3	1.84%
GPR	1.32E-1	8.77E-2	13.72%	1.58E-2	1.01E-2	2.02%
BLS	**3.49E-2**	**2.20E-2**	**3.44%**	**3.15E-3**	**1.96E-3**	**0.39%**

Table 2. Errors of probability distribution functions of atc in the 300-bus system obtained by different methods.

Method	PDF Error			CDF Error		
	RMSE	MAE	WAPE	RMSE	MAE	WAPE
PCE	1.22E-1	8.59E-2	10.73%	1.31E-2	9.16E-3	1.83%
GPR	1.01E+0	6.00E-1	75.07%	8.52E-2	5.48E-2	10.97%
BLS	**5.42E-2**	**3.78E-2**	**4.72%**	**5.50E-3**	**3.64E-3**	**0.73%**

Table 3. Errors of probability distribution functions of atc in the 1354-bus system obtained by different methods.

Method	PDF Error			CDF Error		
	RMSE	MAE	WAPE	RMSE	MAE	WAPE
PCE	-	-	-	-	-	-
GPR	-	-	-	1.58E-1	9.22E-2	18.44%
BLS	**1.87E-2**	**1.27E-2**	**3.65%**	**4.80E-3**	**2.98E-3**	**0.60%**

B. Comparison of Statistical Index Accuracy

Table 4-Table 6 show the statistical indices of ATC obtained by different methods. The errors in the mean for all methods are small, indicating that calculating the mean is not a challenging task. However, the errors in the standard deviation and percentiles obtained by the GPR method increase significantly as the system scale grows. This is because the GPR model tends to output the mean value when the system scale increases, resulting in accurate mean estimation but poor performance in capturing higher-order statistical indices. The PCE method achieves significantly higher accuracy in statistical indices compared to the GPR method, but it fails to compute PATC in the 1354-bus system due to memory limitations. In contrast, the proposed BLS method yields more accurate statistical indices in most cases than both the PCE and GPR methods. This improvement is attributed to the high accuracy of the PDFs and CDFs produced by the BLS method, as demonstrated in Figures 3-5.

Table 4. Statistical indices of atc in the 118-bus system obtained by different methods.

Method	Mean (MW)	Standard Deviation (MW)	5_{th} Percentile (MW)	95_{th} Percentile (MW)
MCS	154.50	19.45	125.70	189.17
PCE	154.56	18.45	**125.62**	186.72
GPR	**154.52**	17.94	126.40	185.95
BLS	154.57	**19.51**	125.04	**189.15**

Table 5. Statistical indices of atc in the 300-bus system obtained by different methods.

Method	Mean (MW)	Standard Deviation (MW)	5_{th} Percentile (MW)	95_{th} Percentile (MW)
MCS	248.74	15.54	224.30	274.66
PCE	**248.71**	14.06	225.80	271.94
GPR	248.51	6.72	237.41	259.81
BLS	248.95	**15.06**	**223.78**	**274.08**

Table 6. Statistical indices of atc in the 1354-bus system obtained by different methods.

Method	Mean (MW)	Standard Deviation (MW)	5_{th} Percentile (MW)	95_{th} Percentile (MW)
MCS	851.13	35.77	795.23	914.27
PCE	-	-	-	--
GPR	**851.02**	11.23	849.14	851.85
BLS	851.55	**35.05**	**795.78**	**912.35**

C. *Comparison of Computational Efficiency*

Figure 6(a)-Figure 6(c) show the computation time for PATC using different methods in the three test systems. The speedup ratio is evaluated by comparing each method with the benchmark based on the MCS method. Since the PCE method fails to complete the PATC calculation in the 1354-bus system due to an out-of-memory issue, Figure 6(c) does not include the computation time for the PCE method. In the 118-bus system, the parameter estimation time for the BLS model is longer than that for the PCE and GPR methods. Hence, the speedup ratio of the BLS method is slightly lower than that of the PCE and GPR methods. However, the parameter estimation time for the PCE model increases rapidly with system scale. Consequently, the PCE method yields the lowest speedup ratio in the 300-bus system and even fails to perform PATC calculations in the 1354-bus system due to memory limitations. As the system scale increases, the speedup ratio of the proposed BLS method improves and becomes comparable to that of the GPR method. In the 1354-bus system, the difference in speedup ratios between the GPR and BLS methods is minimal. Overall, the BLS method demonstrates significant advantages in efficiency and accuracy for PATC calculation, particularly in large-scale systems.

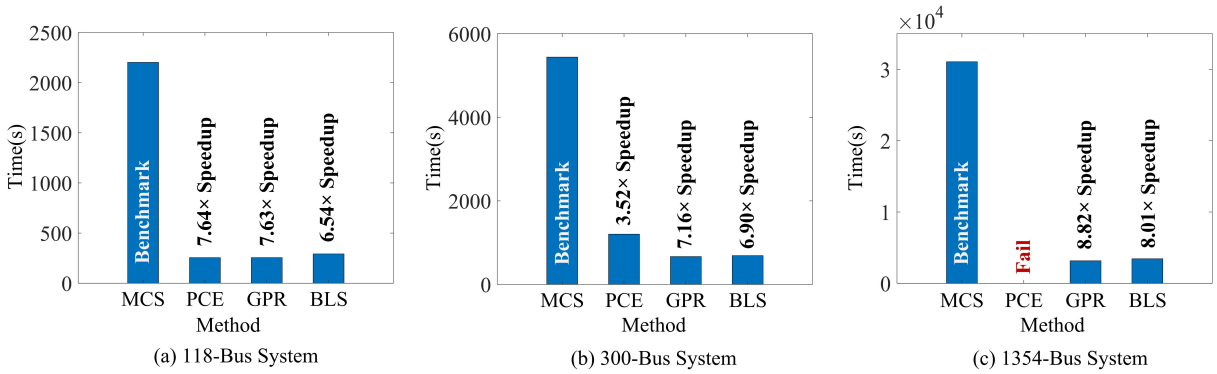

(a) 118-Bus System (b) 300-Bus System (c) 1354-Bus System

Figure 6. Comparison of computation time among different methods.

6. Conclusion

This paper proposes a PATC calculation method by integrating a BLS with GMM-based clustering. A BLS model is designed to serve as a surrogate for the OPF-based ATC calculation model. An improved GMM-based clustering approach, derived by reducing the number of Gaussian components of the kernel density estimation model, is developed to generate high-quality training samples. Subsequently, PATC can be calculated by implementing MCS on the BLS-based ATC surrogate model rather than the original OPF-based ATC calculation model. The 118-bus, 300-bus, and 1354-bus power systems are used to evaluate the performance of the proposed BLS method and compare it with the PCE-based and GPR-based surrogate model methods. On the 118-bus and 300-bus systems, the distribution function errors obtained by the proposed method are less than 50% of those produced by the PCE and GPR methods, while a comparable speedup to the GPR method is also maintained. On the large-scale 1354-bus system, the proposed method overcomes the scalability challenges faced by both the PCE and GPR methods. In future research, we will focus on extending the BLS-based PATC calculation method to incorporate the uncertainties arising from the transmission line and equipment failures.

Fund

This work is supported by Central China Branch of State Grid Corporation of China under Science and Technology Project (52140024000D).

References

[1] G.C. Ejebe, J. Tong, J.G. Waight, J.G. Frame, X. Wang, W.F. Tinney. Available transfer capability calculations. IEEE Transactions on Power Systems, 1998, 13(4), 1521–1527. DOI: 10.1109/59.736300

[2] V. Arabzadeh, R. Frank. Creating a renewable energy-powered energy system: Extreme scenarios and novel solutions for large-scale renewable power integration. Applied Energy, 2024, 374, 124088. DOI: 10.1016/j.apenergy.2024.124088

[3] H.J. Zhang, T. Ding, Y.G. Sun, Y.H. Huang, Y.K. He, C. Huang, et al. How does load-side re-electrification help carbon neutrality in energy systems: cost competitiveness analysis and life-cycle deduction. Renewable and Sustainable Energy Reviews, 2023, 187, 113745. DOI: 10.1016/j.rser.2023.113745

[4] H.X. Dong, Q.Y. Deng, C.J. Li, N. Liu, W.Z. Zhang, M.Y. Hu, et al. A comprehensive review on renewable power-to-green hydrogen-to-power systems: Green hydrogen production, transportation, storage, re-electrification and safety. Applied Energy, 2025, 390, 125821. DOI: 10.1016/j.apenergy.2025.125821

[5] X. Kou, F. Li. Interval optimization for available transfer capability evaluation considering wind power uncertainty. IEEE Transactions on Sustainable Energy, 2020, 11(1), 250–259. DOI: 10.1109/TSTE.2018.2890125

[6] J.W. Stahlhut, G.T. Heydt. Stochastic-algebraic calculation of available transfer capability. IEEE Transactions on Power Systems, 2007, 22(2), 616–623. DOI: 10.1109/TPWRS.2007.894865

[7] A.B. Rodrigues, M.G. Da Silva. Probabilistic assessment of available transfer capability based on Monte Carlo method with sequential simulation. IEEE Transactions on Power Systems, 2007, 22(1), 484–492. DOI: 10.1109/TPWRS.2006.887958

[8] A.B. Khairuddin, S.S. Ahmed, M.W. Mustafa, A.A.M.

Zin, H. Ahmad. A novel method for ATC computations in a large-scale power system. IEEE Transactions on Power Systems, 2004, 19(2), 1150–1158. DOI: 10.1109/TPWRS.2004.825933

[9] Transmission Transfer Capability Task Force, Available transfer capability definitions and determination. North American Electric Reliability Council, Princeton, NJ, USA, Jun. 1996.

[10] P.W. Pande, S. Kumar, A.K. Sinha. Total transfer capability calculation using modified repeated power flow method. 2015 Annual IEEE India Conference (INDICON), 2015, 1–6. DOI: 10.1109/INDICON.2015.7443378

[11] H.D. Chiang, A.J. Flueck, K.S. Shah, N. Balu. CPFLOW: a practical tool for tracing power system steady-state stationary behavior due to load and generation variations. IEEE Transactions on Power Systems, 1995, 10(2), 623–634. DOI: 10.1109/59.387897

[12] A. Suresh, M.S. Hasan, S. Kamalasadan, S. Paudyal. A distributed energy resources integrated transmission and distribution continuation power flow model with sequence component approach. IEEE Transactions on Industry Applications, 2025, 61(4), 1–12. DOI: 10.1109/TIA.2025.3544982

[13] G. Hamoud. Assessment of available transfer capability of transmission systems. IEEE Transactions on Power Systems, 2000, 15(1), 27–32. DOI: 10.1109/59.852097

[14] H. Khaloie, M. Dolányi, J.F. Toubeau, F. Vallée. Review of machine learning techniques for optimal power flow. Applied Energy, 2025, 388, 125637. DOI: 10.1016/j.apenergy.2025.125637

[15] X.T. Wang, X.Z. Wang, H. Sheng, X. Lin. A data-driven sparse polynomial chaos expansion method to assess probabilistic total transfer capability for power systems with renewables. IEEE Transactions on Power Systems, 2021, 36(3), 2573–2583. DOI: 10.1109/TPWRS.2020.3034520

[16] X. Sun, Z.B. Tian, Y.F. Rao, Z.H. Li, P. Tricoli. Probabilistic available transfer capability assessment in power systems with wind power integration. IET Renewable Power Generation, 2020, 14(11), 1912–1920. DOI: 10.1049/iet-rpg.2019.1383

[17] B. Sudret, S. Marelli, J. Wiart. Surrogate models for uncertainty quantification: an overview. European Conference on Antennas and Propagation (EUCAP), 2017, 793–797. DOI: 10.23919/EuCAP.2017.7928679

[18] T. Crestaux, O. Le Maıˆtre, J.M. Martinez. Polynomial chaos expansion for sensitivity analysis. Reliability Engineering & System Safety, 2009, 94(7), 1161–1172. DOI: 10.1016/j.ress.2008.10.008

[19] E. Schulz, M. Speekenbrink, A. Krause. A tutorial on Gaussian process regression: modelling, exploring, and exploiting functions. Journal of Mathematical Psychology, 2018, 85, 1–16. DOI: 10.1016/j.jmp.2018.03.001

[20] S. Marelli, B. Sudret. UQLab: a framework for uncertainty quantification in MATLAB. presented at the 2nd International Conference on Vulnerability and Risk Analysis and Management, Liverpool, United Kingdom, 2014, 2554–2563. DOI: 10.1061/9780784413609.257

[21] A. Wächter, L.T. Biegler. On the implementation of an interior-point filter line-search algorithm for large-scale nonlinear programming. Mathematical Programming, 2006, 106(1), 25–57. DOI: 10.1007/s10107-004-0559-y

[22] H. Sheng, X.Z. Wang. Probabilistic power flow calculation using non-intrusive low-rank approximation method. IEEE Transactions on Power Systems, 2019, 34(4), 3014–3025. DOI: 10.1109/TPWRS.2019.2896219

[23] C.L.P. Chen, Z.L. Liu. Broad learning system: an effective and efficient incremental learning system without the need for deep architecture. IEEE Transactions on Neural Networks and Learning Systems, 2018, 29(1), 10–24. DOI: 10.1109/TNNLS.2017.2716952

[24] C.Y. Lei, J.F. Guo, C.L.P. Chen. ConvBLS: an effective and efficient incremental convolutional broad learning system combining deep and broad representations. IEEE Transactions on Artificial Intelligence, 2024, 5(10), 5075–5089. DOI: 10.1109/TAI.2024.3403953

[25] F. Chu, T. Liang, C.L.P. Chen, X. Wang, X. Ma. Weighted broad learning system and its application in nonlinear industrial process modeling. IEEE Transactions on Neural Networks and Learning Systems, 2020, 31(8), 3017–3031. DOI: 10.1109/TNNLS.2019.2935033

[26] X.R. Gong, T. Zhang, C.L.P. Chen, Z.L. Liu. Research review for broad learning system: algorithms, theory, and applications. IEEE Transactions on Cybernetics, 2022, 52(9), 8922–8950. DOI: 10.1109/TCYB.2021.3061094

[27] N. Zhou, X.Y. Xu, Z. Yan, M. Shahidehpour. Spatio-temporal probabilistic forecasting of photovoltaic power based on monotone broad learning system and copula theory. IEEE Transactions on Sustainable Energy, 2022, 13(4), 1874–1885. DOI: 10.1109/TSTE.2022.3174012

[28] K.K. Xu, T.L. He, P. Yang, X.B. Meng, C.J. Zhu, X. Jin. A new online SOC estimation method using broad learning system and adaptive unscented Kalman filter algorithm. Energy, 2024, 309, 132920. DOI: 10.1016/j.energy.2024.132920

[29] M.G. Gong, J. Liu, H. Li, Q. Cai, L.Z. Su. A multiobjective sparse feature learning model for deep neural networks. IEEE Transactions on Neural Networks and Learning Systems, 2015, 26(12), 3263–3277. DOI: 10.1109/TNNLS.2015.2469673

[30] L. Yu, T.Y. Yang, A.B. Chan. Density-preserving hierarchical EM algorithm: simplifying Gaussian mixture models for approximate inference. IEEE Transactions on Pattern Analysis and Machine Intelligence, 2019, 41(6), 1323–1337. DOI: 10.1109/TPAMI.2018.2845371

[31] Y.H. Gao, X.Y. Xu, Z. Yan, M. Shahidehpour. Gaussian mixture model for multivariate wind power based on kernel density estimation and component number reduction. IEEE Transactions on Sustainable Energy, 2022, 13(3), 1853–1856. DOI: 10.1109/TSTE.2022.3159391

[32] R.D. Zimmerman, C.E. Murillo-Sánchez, R.J. Thomas. MATPOWER: steady-state operations, planning, and analysis tools for power systems research and education. IEEE Transactions on Power Systems, 2011, 26(1), 12–19. DOI: 10.1109/TPWRS.2010.2051168